Applied Catalysis B: Environmental 336 (2023) 122917

Contents lists available at ScienceDirect

Applied Catalysis B: Environmental

journal homepage: www.elsevier.com/locate/apcatb

The asymmetric orbital hybridization in single-atom-dimers for urea synthesis by optimizing the C-N coupling reaction pathway

Chongchong Liu [a,1], Haili Tong [b,c,1], Peifang Wang [a,*], Rong Huang [a], Peilin Huang [a], Gang Zhou [a,*], Lizhe Liu [d,*]

[a] Key Laboratory of Integrated Regulation and Resource Development on Shallow Lake of Ministry of Education, College of Environment, Hohai University, Nanjing 210098, People's Republic of China
[b] PKU-HKUST ShenZhen-HongKong Institution, Shenzhen 518057, People's Republic of China
[c] Beijing National Laboratory for Molecular Science, Key Laboratory for the Physics and Chemistry of Nanodevices, State Key Laboratory of Rare Earth Materials Chemistry and Applications, College of Chemistry and Molecular Engineering, Peking University, Beijing 100871, People's Republic of China
[d] Jiangsu Key Laboratory for Nanotechnology and Collaborative Innovation Center of Advanced Microstructures, National Laboratory of Solid State Microstructures, Nanjing University, Nanjing 210093, People's Republic of China

ARTICLE INFO

Keywords:
Urea synthesis
Dual single atom
Asymmetric catalytic
C-N coupling

ABSTRACT

Electrocatalytic reduction from nitrate (NO_3^-) and carbon dioxide (CO_2) parades great prospects in substituting traditional process for urea synthesis, but challenges remain due to the arduous C-N coupling and multistage protonation. Unlike common design strategies, our study utilized synergistic effect between asymmetrical sites to reduce coupling barrier and promote urea production. Herein, we anchor dual single-atom Ru and Co on N-doped carbon for fixing the C/N group respectively and minimizing the generation energy for intermediates. As a result, the $CoRuN_6$ electrocatalyst successfully restricts the parrel reaction (CO_2/NO_3^- reduction) and affords a urea yield of 8.98 mmol $h^{-1}g^{-1}$ and a faradic efficiency (FE) of 25.31% at − 0.6 V versus RHE. Our research provides novel insights into capitalizing on spatial regulation of active sites for efficient urea electrosynthesis.

1. Introduction

Urea ($CO(NH_2)_2$) is both the pivotal nitrogen fertilizer for crop growth and a crucial feedstock for synthesizing common chemicals such as urea formaldehyde, melamine, and barbiturates [1,2]. For the huge demand, traditional Bosch-Meiser process is massively utilized in the industrial urea fabrication, but facing grand restraints of high energy consumption (1–2% of global entirety) and severe reaction conditions (150–200 °C, 150–250 bar) [3,4]. Worse still, the low urea production efficiency from ammonia (NH_3) and carbon dioxide (CO_2) also engenders the squandering of nitrogen resources and emission of greenhouse gases [5]. In recent years, electrocatalytic urea synthesis has been proposed as a promising alternative for traditional methods, in which CO_2 flow reacts with nitrogen (N_2), nitrite (NO_2^-) or nitrate (NO_3^-) under mild temperature and steady voltage [4,6]. Among these, the direct conjugation of CO_2 and NO_3^- (abundant eutrophication pollutants) for producing urea can simultaneously play a significant role in mitigating greenhouse effect, sustain ecology nitrogen balance, alleviating the energy crisis [7].

It has been reported that the urea synthesis from CO_2 and nitrate is thermodynamic spontaneous and theoretically feasible [8]. Nevertheless, due to the intricate proton-coupling electron-transfer (PCET) containing 16 electrons transfer, its selectivity is inevitably lower than the parallel NO_3^- reduction reaction (NO_3RR) or CO_2 reduction reaction (CO_2RR), essentially restricting urea synthesis efficiency [9]. Although the bicarbonate (HCO_3^-) assistance can effectively accelerate proton-coupling, it also actually exacerbates voltage consumption and hydrogen evolution reaction (HER) [10]. Moreover, two C-N coupling processes (key steps) during the urea generation are often accompanied with high energy barrier, substantially hindering the reaction kinetics [7,11]. Regarding these obstacles, numerous novel catalysts have been designed to promote co-activation of CO_2 and NO_3^- for higher urea selectivity and yield [12,13]. The previous works mainly focus on enhancing catalytic sites activity to fix CO_2, NO_3^- or key intermediates, pursuing higher C-N coupling frequency [14,15]. Unfortunately, few attentions are concentrated on optimizing the spatial configuration

* Corresponding authors.
E-mail addresses: pfwang2005@hhu.edu.cn (P. Wang), gangzhou@hhu.edu.cn (G. Zhou), lzliu@nju.edu.cn (L. Liu).
[1] These authors contributed equally to this work.

https://doi.org/10.1016/j.apcatb.2023.122917
Received 26 April 2023; Received in revised form 9 May 2023; Accepted 24 May 2023
Available online 26 May 2023
0926-3373/© 2023 Elsevier B.V. All rights reserved.

between sites and products to accelerate electron transfer and reduce reaction barrier. It is accepted that the C-N coupling is inclined to occur when the C/N intermediates are anchored on neighboring sites respectively [8,16]. Notably, the selectivity of active sites to C/N species is often rivaling, which also decides its tendency for CO_2RR or NO_3^-RR [17,18]. Once C and N reactants respectively adsorbed on two symmetrical sites with equivalent activity, the coupling product is hard to maintain spatial stability by virtue of its own asymmetry. It can be reasonably inferred that the site connected to low-selective reactants probably declines adsorption energy on products after C-N coupling. Then, the released site may occur CO_2RR or NO_3^-RR reaction individually, lowing the utilization of sites for urea synthesis. On the contrary, C-N coupling product can be simultaneously anchored on two asymmetry sites and keep spatial balance driven by the strong bonding interactions when C/N reactants are adsorbed on two sites with high CO_2RR and NO_3^-RR preference respectively. This asymmetry configuration based on C/N selectivity difference can entirely occupy dual sites, enhance the intermediates adsorption and accelerate interfacial electron transfer, conducive to the following PCET process and urea fabrication [19,20].

Herein, we report a bimetallic catalyst ($CoRuN_6$) anchored on polymeric carbon nitride via a facile strategy for efficient urea electrocatalytic synthesis. Our design is based on the following considerations: (1) Dual single-atom catalysts (DSACs) can regulate the different coordination environment to control the distance between sites, exploring stable environment for C-N coupling [21,22]. (2) DSACs comprising adjacent metal active sites can build a possible bridge-cis adsorption model on intermediates and promote electron transfer efficiency, which is deemed to favor the PCET process [23]. (3) Co and Ru atoms are reported as excellent sites for NO_3^-RR and CO_2RR, respectively, favorable to build the asymmetry system for C-N coupling and verify our hypothesis (Fig. 1a) [24,25]. As expected, the resultant catalyst exhibited superior urea yield (8.98 mmol $h^{-1}g^{-1}$) with high Faradaic efficiency (FE, 25.31%), obviously outperforming catalyst merely with Ru or Co site (CoN_4 and RuN_4). Both the in-situ characterization and theoretical calculation unveil that the asymmetry configuration induced by dual sites can significantly optimize intermediate (*CO_2NO_2) bonding, contributing for higher urea selectivity. It can also thermodynamically accelerate the most energy-demanding reaction step (dehydroxylating for *$COOHNH_2$) and kinetically minimize energy barriers for two C-N couplings (0.62 and 0.44 eV).

2. Experiment section

2.1. Preparation of CoN_4, RuN_4, and $CoRuN_6$

All involved chemicals are in analytical grade and used without further purifications. The novel catalysts were prepared via a hybrid pyrolysis method. Typically, 24.91 mg $Co(Ac)_2{\cdot}4\,H_2O$ and 27.82 mg $Ru(Ac)_3$ were mixed into 50 mL ethanol. Then, 37 mg 2,6-diacetylpyridine, 50 mg 2,6-diacetylpyridine, and 400 mg carbon blacks were added and alternately sonicated and stirred for 2 h. Subsequently, the mixture was heated on an oil bath with magnetic stirring at 80 °C until the solvent was totally evaporated. The obtained pyridine precipitates were moved to a mortar and ground with a pestle for 15 min, then heated up and

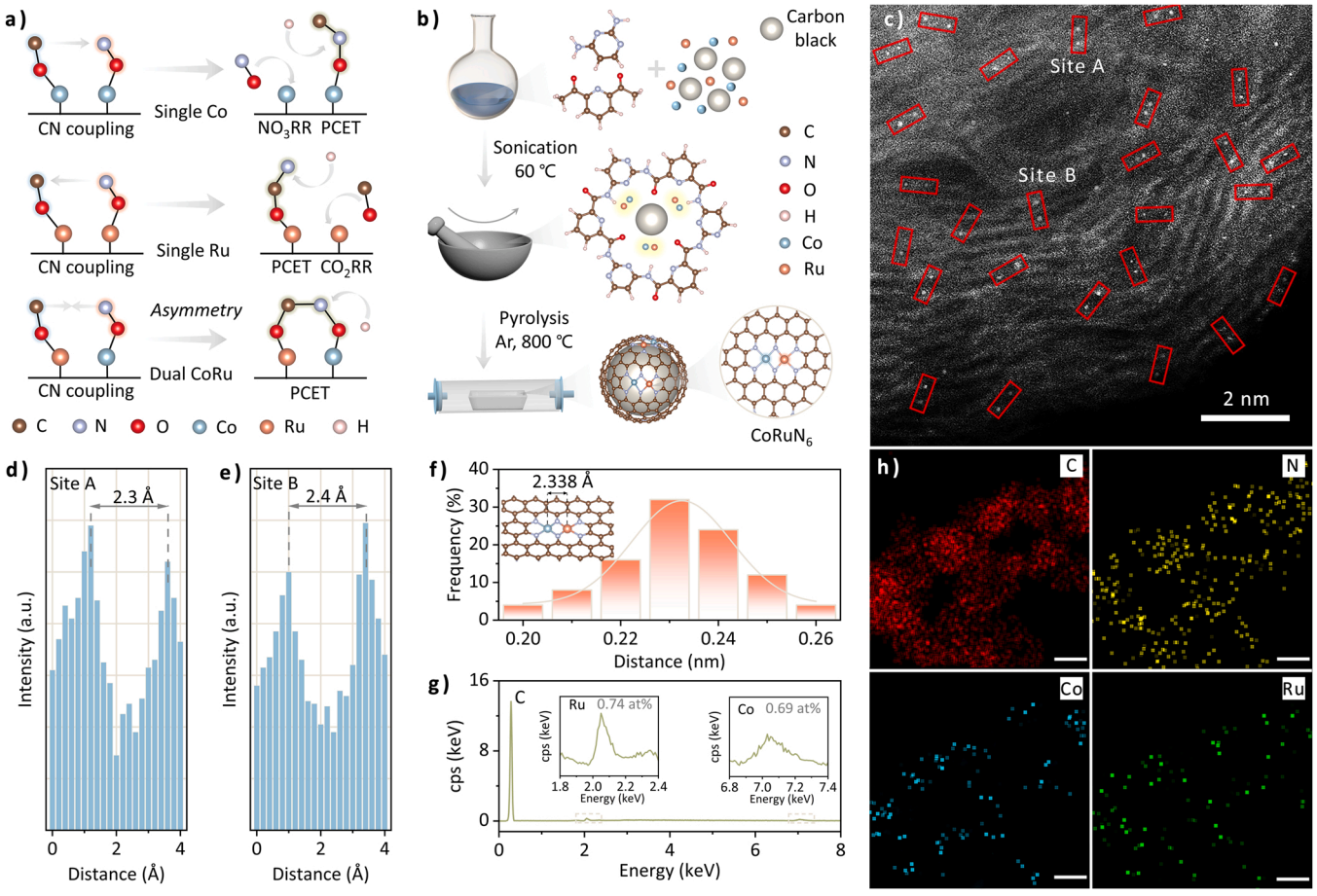

Fig. 1. (a) Schematic illustration of C-N coupling process on single and dual sites. (b) Diagram for synthetic procedure of $CoRuN_6$. (c) Aberration-corrected HAADF-STEM image of $CoRuN_6$. (d, e) Line-scanning intensity profile on bimetallic site A and B in image b. (f) Statistical Ru-Co distance in the observed diatomic pairs (inset: calculated distance between Ru and Co atom in simulated model). (g) EDS spectrum (inset: mass fraction calculated from ICP-MS) and (h) corresponding elemental mapping images of $CoRuN_6$ (scale bar: 50 nm).

pyrolyzed in a tube furnace to 800 ℃ under an Ar atmosphere for 2 h. The $CoRuN_6$ powder was finally obtained after underwent acid leaching to remove extra metallic species. The CoN_4 and RuN_4 were synthesized via same methods except that the metal reactants were replaced by 49.82 mg $Co(Ac)_2{\cdot}4\ H_2O$ and 55.64 mg $Ru(Ac)_3$, respectively.

2.2. Urea electrosynthesis

Electrochemical measurements were operated on an electrochemical work station (CIMPS, Zahner, Germany) with a three-electrode system. The catalyst ink containing 5 mg of sample, 40 μl Nafion solution (5 wt %), 480 μl of H_2O, and 480 μl H_2O of ethanol was sonicated for 40 min and then 40 μl of ink was dropped on a carbon paper as a working electrode. Its catalytic area was 1.0 × 1.0 cm^2 and the mass loading was 0.2 mg cm^{-2}. Platinum sheet and Ag/AgCl electrodes were utilized as counter and reference electrodes, respectively. The urea electrosynthesis was carried on in a H-cell reactor containing 50 mL of KNO_3 (0.1 M) via a chrono amperometry mode with a steady voltage (−0.4, −0.5, −0.6, −0.7 V). CO_2 (>99.999%) airflow was constantly injected into the closed system at a rate of 30 mL min^{-1} and bubbling for 20 min to reach saturation before testing. The electrochemical process was performed in cathode reaction chamber and maintained 2 h with magnetic stirring of 500 rpm (shown in Fig. S1). The linear sweep voltammetry (LSV) curves were tested under the same condition and the scan rate was 10 mV s^{-1}. All measured potentials were versus Ag/AgCl and transformed to reversible hydrogen electrode (RHE) potential by equation:

$$E_{RHE} = E_{Ag/AgCl} + 0.0591 \times pH + 0.197 \quad (1)$$

More details about the products quantification in electrocatalytic reactions were seen in Text S1 and S2 in supporting information.

2.3. Computational Method

The DFT calculation methods on the electronic structure and Gibbs free energy are carried out by first-principles theory via the Vienna Abinitio Simulation Package (VASP) code [26]. The exchange-functional is treated using the generalized gradient approximation (GGA) of Perdew-Burke-Ernzerhof (PBE). The kinetic energy cutoff for the plane wave basis was 450 eV. Brillouin zone integration on grids with 3 × 3 × 1 Monkhorst-Pack k-points was implemented for geometrical optimization and calculation of density of states. The convergence criterion for the electronic self-consistent iteration and force were set to 10^{-5} eV and 0.02 eV/Å. The vacuum layer in the slab model is larger than 15 Å to avoid superficial interaction between periodical slabs and the intermediates were built on the surface for structural relaxation. The free energy (ΔG) of each adsorbed intermediate is calculated as

$$\Delta G = \Delta E + \Delta E_{ZPE} - T\Delta S \quad (2)$$

where ΔE, ΔE_{ZPE}, and ΔS respectively represent the changes of electronic energy, zero-point energy, and entropy that caused by adsorption of intermediate. The thermodynamic corrections at the reaction temperature (300 K) were evaluated by using VASPKIT software [27]. The climbing image nudged elastic band (CINEB) method with 8 sites inserted was used to find transition states and obtain the energy barriers [28]. The crystal orbital Hamilton population (COHP) was extracted via the software lobster 4.1.0 [29].

3. Results and discussion

3.1. Structure characterization

As schematically illustrated in Fig. 1b, we implanted the Co/Ru dual sites on N-doped carbon via a facile strategy with sonication and pyrolysis (details shown in Section 2.1). After obtaining the designed catalysts (CoN_4, RuN_4, $CoRuN_6$), multiple structure characterizations and theoretical modeling were conducted for investigation at the micro level. The crystalline structures of the as-prepared catalysts were analyzed by X-ray diffraction (XRD). As revealed in Fig. S2, two obvious peaks at 25° and 44° were observed in all samples, indexed to the (002) and (101) crystal planes of graphitic carbon, respectively [30]. No other apparent signals were detected, explicating that metal Co/Ru may be atomically dispersed in catalysts [31]. It can also be verified by the fact that no metal nanoparticles were noticed in STEM images (Fig. S3). To further exclude the possibility of metal clusters, Aberration-corrected HAADF-STEM was carried out to investigate the distribution at higher magnification. As exhibited in Fig. 1c, numerous bright spots with Ångstrom size are evenly distributed on carbon matrix and dominantly appeared in pairs (marked by red box). It is attributed to the larger contrast of metal atoms under dark field, suggesting the Co and Ru sites were dispersed in the form of atoms instead of clusters [32]. The line-scanning profile of region A and B (Figs. 1d and 1e) enlarged the two neighboring atoms with slightly different intensity and proved the existence of Co-Ru dual single-atom sites [33]. After ruling out few single-atom sites, the statistical interatomic distance of observed Co-Ru sites was 2.3 ± 0.3 Å (Fig. 1 f), which is in high approximation with the results from theoretical calculated (2.338 Å, Fig. S4). Additionally, Energy dispersive X-ray spectroscopy (EDS, Fig. 1 g) spectrum captured the slight signals of Co and Ru (0.74 and 0.69 at%) and their atomic ratio is approximately 1:1, corresponded to the results from inductively coupled plasma-mass spectrometry (ICP-MS, Table S1). The relating EDS element mapping (Fig. 1 h) signified the homogeneous dispersion of Co-Ru dual single-atom sites on the entire catalysts, conduced to the efficient utilization of active sites.

In order to further characterize the element state and atomic coordination environment of $CoRuN_6$ accurately, synchrotron radiation X-ray absorption spectroscopy (XAS) was performed. The X-ray absorption near-edge structure (XANES) profiles (Fig. 2a) magnified the normalized absorption edge of Co/Ru K-edge in $CoRuN_6$ with standards as reference. Herein, Co K-edge was positioned between CoO and Co_3O_4, suggesting that the average Co valence state is between Co(II) and Co(III) [34]. Similarly, the chemical valence of Ru is ranging from 0 to + 4, owing to the fact that its K-edge was located between Ru foils and RuO_2 (inset). Meanwhile, the Fourier transform extended X-ray absorption fine structure (FT-EXAFS) disclosed the predominant peak at ~1.5 Å upon R space curves for Co and Ru K-edge (Figs. 2b and 2c), corresponding to the Co-N and Ru-N bond scattering [35,36]. The absence of significant Ru-Ru/Co-Co signals in the 2nd coordinated shell (2–6 Å) of R space further verified the atomically dispersed form of Co and Ru, in line with the HAADF- STEM observation. Additionally, the Ru-Co peak was also not noticed, excluding the possibility of Ru-Co clusters or Ru-Co bond in $CoRuN_6$. To explain the metal coordination path, wavelet transform (WT)-EXAFS was also conducted in k-space resolution (Fig. 2d). Distinguished from the Co-O or Ru-O bonding in other catalysts, the intensity center of Co-N and Ru-N in $CoRuN_6$ were both at ~4 $Å^{-1}$, matching the coordination numbers from least-squares EXAFS fitting (4.0 and 3.9, Table S1). The best fitting results with theoretical model (Fig. 2e and Fig. S5) also demonstrated the unique CoRu-N_6 structure, in which Co/Ru dual single atoms were inner-connected by two nitrogen atoms, as we expected. Moreover, density functional theory (DFT) calculations proved that this atom coordination can minimize interatomic distance simultaneously promote the bader charge distribution on Co/Ru atoms (Fig. 2 f), consistent with the binding energy shifts in XPS results (Fig. S6). Affected by this, D-band center of $CoRuN_6$ was induced closer to Fermi level (−0.495 eV) and the partial density of states (PDOS) around Fermi level was enhanced (Fig. S7), conductive to the bonding state occupation and electron releasing in electrocatalytic reduction reaction [37]. In summary, the as-prepared $CoRuN_6$ catalyst paraded potential benefits in urea synthesis from the perspective of spatial configuration and electronic structure.

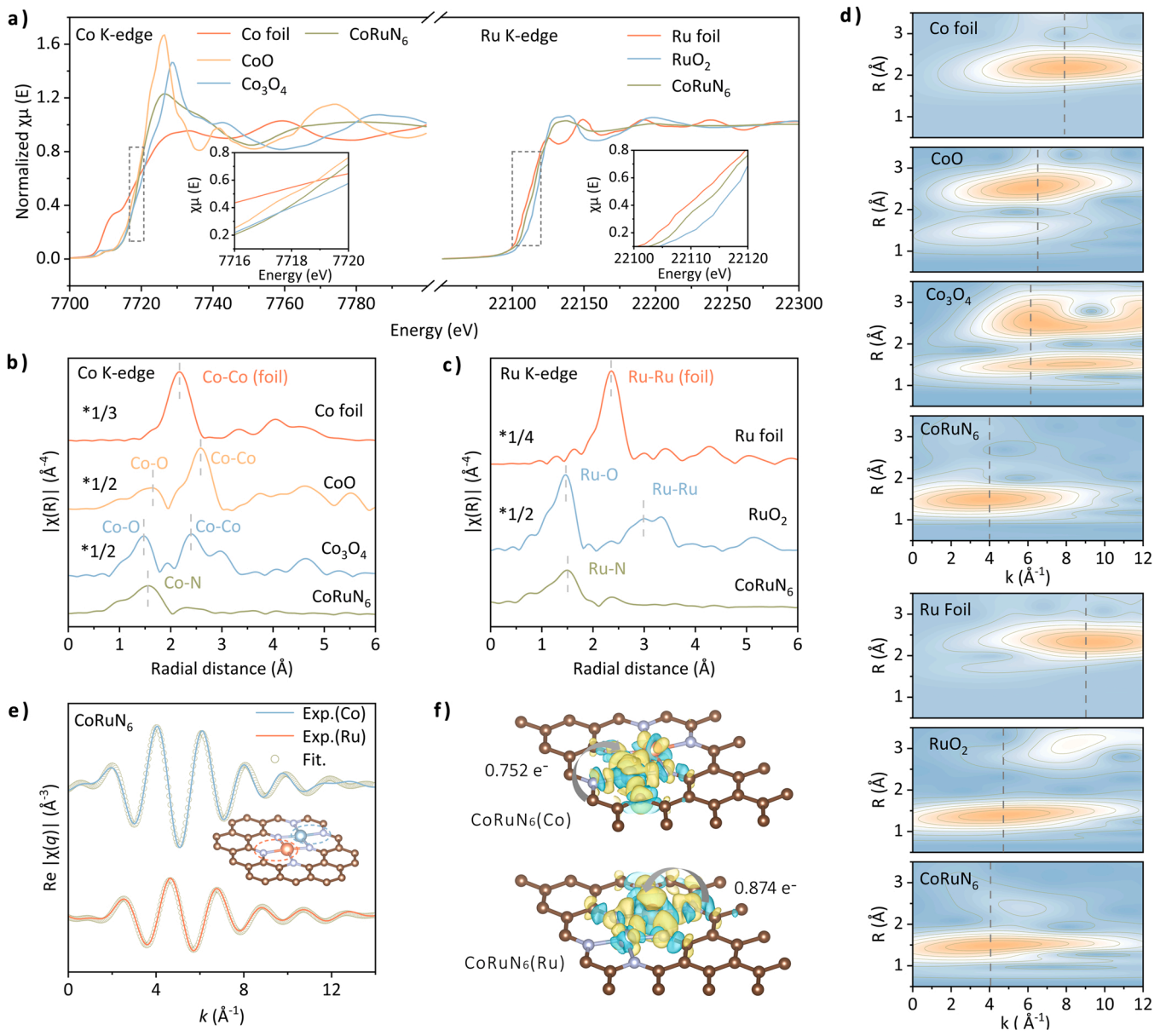

Fig. 2. (a) Normalized Co and Ru K-edge XANES spectra of different samples. (b, c) Fourier transforms of k^3-weighted Co and Ru K-edge EXAFS spectra of $CoRuN_6$ and references. (d) Wavelet transforms for k^3-weighted EXAFS signals of different samples (up: Co, down: Ru). (e) FT-EXAFS fitting curves in q spaces. (f) Charge density differences of Co and Ru in $CoRuN_6$ simulated structure.

3.2. Electrocatalytic urea synthesis

The electrocatalytic urea synthesis was performed in an H-cell reactor containing 0.1 M KNO_3 and CO_2 stream, relying on chrono amperometry (CA) method at fixed potentials. The urea yield was evaluated by diacetyl monoxime measurement, validated by urease method and NMR quantification (Text S1). As illustrated in Fig. 3a, the urea amount generated by $CoRuN_6$ at various potential was divergent and reached a maximum value at − 0.6 V versus RHE. Its calculated urea yield was 8.98 mmol $h^{-1}g^{-1}$ (Fig. 3b), significantly higher than those of single-atom catalysts (3.16 and 4.97 mmol $h^{-1}g^{-1}$). The related Faradaic efficiencies (FE) for urea electrosynthesis were sketched in Fig. 3c. With increasingly negative potentials, the FE_{urea} of catalysts firstly raised, then gradually declined and $CoRuN_6$ obtained the highest value (25.31%) at − 0.6 V versus RHE, recognized as the optimal voltage for fabricating urea. Considering the yield and FE together, the electrocatalytic urea fabrication performance of $CoRuN_6$ clearly surpassed those of most similar catalysts (CO_2 and NO_3^- as reactants) and some catalysts using N_2 or NO_2^- as nitrogen source (comparison in Fig. 3d). Cyclic tests (Fig. S8) further demonstrated that $CoRuN_6$ exhibited extremely stable performance for urea electro-synthesis. To further clarify the competitive relationship among parallel reactions, we tested the NO_3^-RR, CO_2RR activity and electrochemical parameters under the same reaction condition (details in Text S2). As seen in Fig. 3e, the nitrate (NH_3) and carbon monoxide (CO) were the main products of two side reactions. Notably, CoN_4 and RuN_4 paraded remarkable preference on NH_3 and CO respectively, which is in accordance with our preceding judgement and explained their low yield on urea. Additionally, the $CoRuN_6$ system exposed highest effective current intensity (J, 3.04 mA cm^{-2}, Fig. S10) and double layer capacitance (Cdl, 75.02 mF cm^{-2}, Fig. S11), testifying its superior ability for releasing electrons and consisting with the previous DFT results [11,38]. Aside from CO_2RR, NO_3^-RR, we also measured the related yield for hydrogen evolution (Text S2), and thus obtained the total FE distribution for all products in three catalytic systems, as present in Fig. 3 f. Apparently, the electron selectivity towards NH_3 in CoN_4 is dominant (71.35%), which further

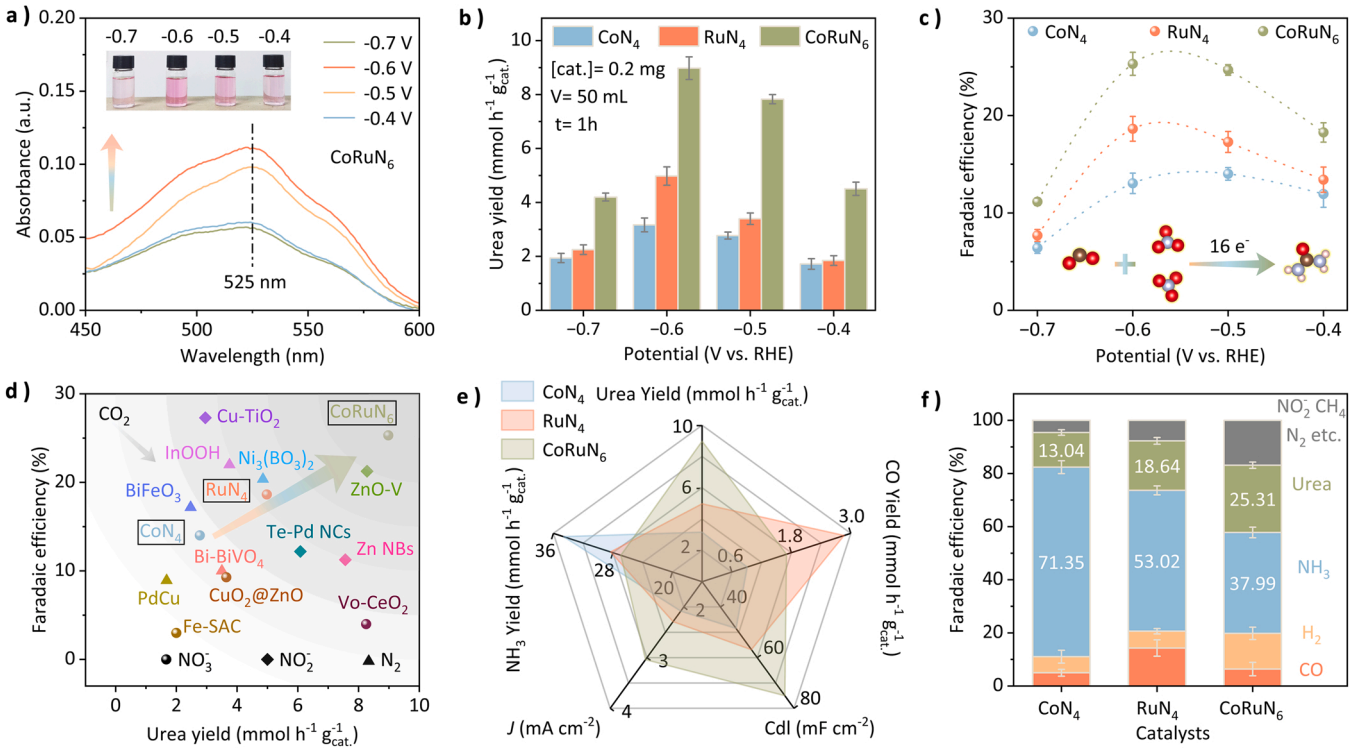

Fig. 3. (a) UV–vis absorption spectra of urea quantification for $CoRuN_6$ in 0.1 M KNO_3 electrolyte with CO_2 flow. (b, c) Urea yields and FE_{Urea} for different catalysts at different potentials. (d) Comparison on urea synthesis performance of as-prepared samples with that of reported catalysts with different nitrogen sources. e) Comparison of urea, NH_3, CO production, current density (*j*) at − 0.6 V versus RHE and calculated Tafel slope from polarization curve. (f) Faradaic efficiencies distribution of all products for different catalysts at − 0.6 V versus RHE. Reaction condition: $[KNO_3] = 0.1$ M, $[CO_2] = 30$ mL min^{-1}.

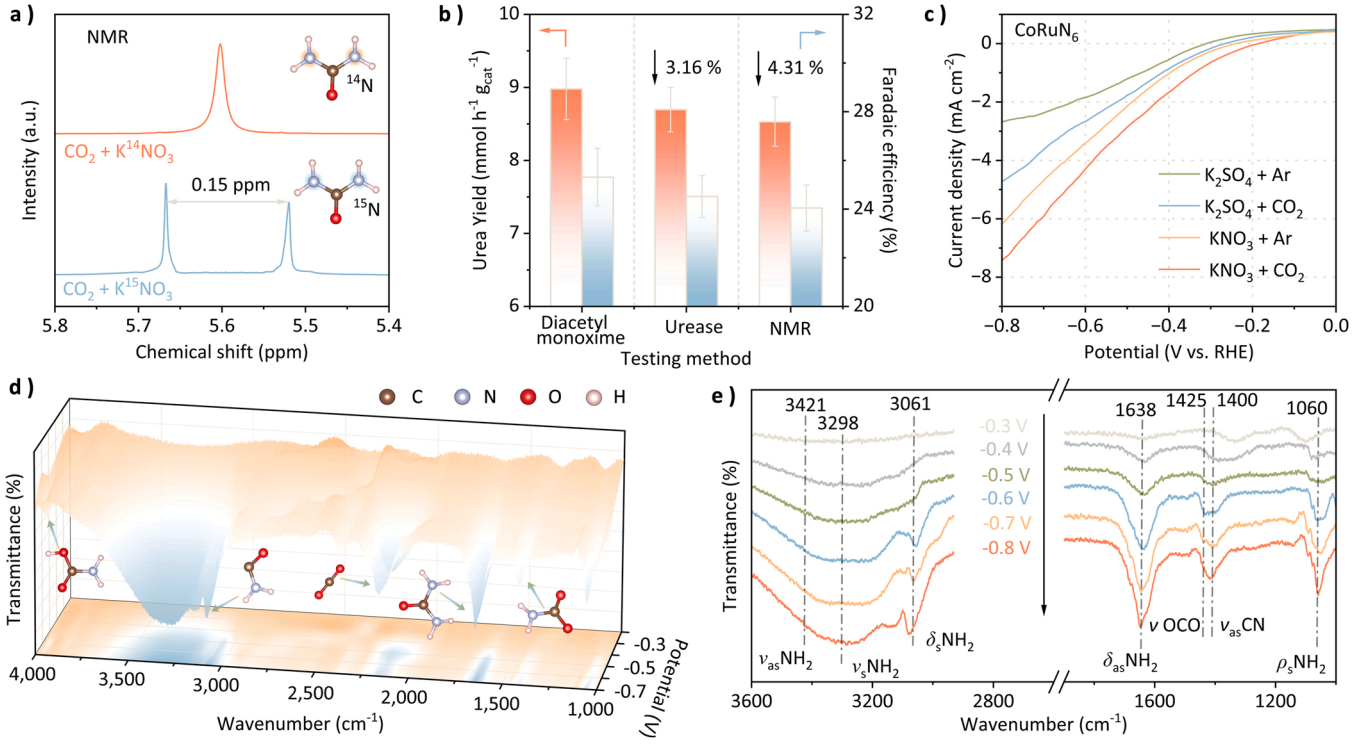

Fig. 4. a) ^1H NMR spectra obtained by using $K^{14}NO_3$ and $K^{15}NO_3$ as the reactants. (b) Urea yield rates and corresponding Faradaic efficiencies obtained by UV–vis spectra method, urease decomposition method and isotope labeling NMR measurements respectively at − 0.6 V versus RHE. (c) LSV curves of $CoRuN_6$ measured in saturated 0.1 M K_2SO_4/KNO_3 electrolytes containing Ar/CO_2 flow. (d) Three-dimensional in-situ FTIR spectra in the range of 1000–4000 cm^{-1} (inset: potential intermediates). (e) infrared signal from 1000 to 3600 cm^{-1} during the electro-coupling of nitrate and CO_2 under various potentials.

boosted under more negative voltage (Fig. S14) and severely hampered urea selectivity. The RuN_4 paraded highest FE_{CO} (14.30%) among catalysts and lower FE_{NH3} (53.02%) than CoN_4. Compared with single-atom catalysts, $CoRuN_6$ drastically reduced the electron selectiveness on NH_3 (37.99%) and CO (6.4%) simultaneously. Then, the partial electrons trended to generate H_2 in HER or by-products in NO_3RR/CO_2RR (grey region) and the remaining (a quarter of total) directly engaged in urea synthesis. In brief, the bimetallic atoms asymmetry system successfully accomplished high urea yield and selectivity via suppressing parallel reactions.

3.3. Dynamic analysis

For the sake of unveiling the dynamic formation process of urea, we subsequently conducted several control experiments with $CoRuN_6$ at − 0.6 V (optimal voltage). Firstly, we synchronously carried out tests in CO_2 saturated 0.1 M $K^{14}NO_3$ and $K^{15}NO_3$ electrolytes and the results were sketched in Fig. 4a. The ^1H NMR spectra distinguished the existing of $^{14}NH_2CO^{14}NH_2$ and $^{15}NH_2CO^{15}NH_2$ products according to the chemical signals from singlet and doublet peaks, respectively [39]. Barely stretching vibrations were observed at ~5.6 ppm in $K^{15}NO_3$ reaction system, confirming that the produced urea is entirely derived from the coupling reaction of CO_2 with NO_3^-, instead of N_2 in air or N atoms in $CoRuN_6$. On the basis of standard curve for urea with N^{15} isotope labeling (Fig. S15), we acquired the urea yield via ^1H NMR and the result was compared with the values calculated by diacetyl monoxime (UV–vis absorbance) and urease method (Fig. S16). As shown in Fig. 4b, the relative error of the three methods was limited lower than 5%. The detection of NO_2^- (Fig. S17) further excluded the false positive possibility attributable to byproduct and verified the accuracy of the experimental results [10,39]. Additionally, the linear sweep voltammetry (LSV) curves of $CoRuN_6$ in different electrolytes were tested and summarized in Fig. 4c. In K_2SO_4/Ar system, the current change with increasingly negative potentials was slight, suggesting the low activity of $CoRuN_6$ on HER and consisting with the previous FE analysis [40]. The current increasing tendency in KNO_3/Ar was higher than that in K_2SO_4/CO_2, ascribed to more electron transfer in NO_3^-RR than CO_2RR. Notably, the KNO_3 electrolyte with saturated CO_2 realized the highest current density, demonstrating that the urea electrosynthesis by $CoRuN_6$ was kinetically most feasible [16,41].

To further monitor the evolution of the bonding structure during the CN-coupling and PCET process, in-situ Fourier transform infrared (FT-IR) were performed on $CoRuN_6$. The infrared signals were collected from 1000 to 4000 cm^{-1} and the applied voltage was ranged from − 0.4 to − 0.9 V versus RHE, as depicted in Fig. 4d and Fig. 4e. Initially, the characteristic peak at ~2300 cm^{-1} (zoomed in Fig. S18a) was assignable to the asymmetric vibration of CO_2, confirming its successive adsorption on $CoRuN_6$ [42]. The vibration at 1400 cm^{-1} from − 0.4 V was attributed to the stretching of C-N bond (ν_{as} CN), symbolizing the co-activation and coupling of CO_2 and NO_3^- [43]. Combing the OCO vibrational band (ν OCO) at 1425 cm^{-1}, we validated the existence of CO_2NO_2 intermediate specie, which was the crucial product in 1st C-N coupling and converted to CO_2NH_2 after PCET reaction [8,44]. The spectra at high wavenumbers captured the distinct OH signal at ~3873 cm^{-1} (enlarged in Fig. S18b), probably ascribed to the intermediates (such as $HOCONH_2$) after hydrogenation reaction [45]. Then, $CONH_2$ specie was observed after hydroxyl shedding and it was the reactant for 2nd C-N coupling and corresponding to the emergence of H-N-H stretching mode (ν_{as} NH_2) and N-H bending mode (δ_s NH_2) at 3298 and 3061 cm^{-1}, respectively [46]. Subsequently, the urea molecular (H_2NCONH_2) was synthesized after 2nd C-N coupling and PCET reactions and exposed unique bending mode and rocking mode of amino (ν_{as} NH_2 and ρ_s NH_2) at 1638 and 1060 cm^{-1}, respectively [43,47]. Totally, the in-situ FTIR measurements explicitly revealed the urea production procedures predicated on multistage coupling and protonation, according well with our previous assumption.

3.4. Theoretical mechanism

The density functional theory calculations were performed to further unravel the fundamental mechanism of electrocatalytic urea synthesis by $CoRuN_6$ from NO_3^- and CO_2. The calculation details were profiled in Section 2.3 and the CoN_4 and RuN_4 were constructed with analogous dual-atom structure for clear comparison. As expound in Fig. 5a, the urea production in $CoRuN_6$ was initiated from the instinctive adsorption of NO_2^- on Co site by Co-O bonding. Then, CO_2 adsorbed on Ru atom coupled with the $*NO_2^-$ and obtained the $*CO_2NO_2$ (step 2), as previously analyzed. After subsequent protonation reactions (step 3–10), the $*CONH_2$ was formed and eventually reduced to urea ($*CO(NH)_2$) after 2nd round C-N coupling and PCET (step 11–12). It is worth noting that the C/N moieties of byproducts were synchronously stabilized on Ru/Co sites in step 2, 5, 7, 10, which was absolutely different form the situation in single atom systems (Fig. S19) and achieved our design aims. These ridge-cis adsorption model reduced the energy of the adsorbed states and boosted electron transfer via the bridge-cis route (Fig. 5b), ultimately promoting urea fabrication [48]. It was also verified by the lower free energy of associated intermediates in $CoRuN_6$ than that in RuN_4/-CoN_4, as listed in Fig. 5c. Herein, the whole reaction was mostly thermodynamic spontaneous and the rate determining step (RDS) was the dehydroxylating of $*COOHNH_2$ (step 9–10), in consonance with the in-situ FT-IR result. Importantly, $CoRuN_6$ exposed lowest energy demand (1.17 eV) for RDS than single-atom structures (1.51 and 1.54 eV). Noting that $*NO_2$ could either be reduced to $*HNO_2$ for further NO_3^-RR, the related free energies were also calculated (see inset). Herein, the $*CO_2NO_2$ formation in $CoRuN_6$ was distinguished from that in RuN_4/-CoN_4 and more thermodynamically favorable (0.59 eV) than $*HNO_2$ (0.77 eV), explaining its restraint on FE_{NH3} and correlating well with LSV analysis [9,49]. Meanwhile, Fig. 5d disclosed that the formation of *COOH and *CO onto $CoRuN_6$ were endothermic and unspontaneous by ΔG of 0.10 and 0.24 eV, corresponding with the limiting effect of $CoRuN_6$ on CO_2RR in electrocatalytic tests [11,50].

In details, the free energy changes during the two C-N couplings were further analyzed via transition states (TS) along the reaction paths (Figs. 5e and 5 f). The activation energy (E_a) in $CoRuN_6$ for the 1st coupling was merely 0.62 eV, significantly lower than those in RuN_4 and CoN_4 (1.27 and 0.91 eV). The situation in 2nd coupling driven by $CoRuN_6$ was resemble, in which $*CONH_2$ and $*NO_2$ rapidly bounded together and converted to $*CONO_2NH_2$ under an ultralow E_a (0.44 eV). Furthermore, the bonding states of O atom in $*CONH_2$ (RDS products) absorbed on catalysts were further extracted by crystal orbital Hamilton population (COHP, Fig. 5 g). The ICOHP in $CoRuN_6$ (−1.06) are significantly higher than in CoN_4 and RuN_4 (−0.40 and −0.72), indicating its strongest bonding interaction and explaining its lowest energy barrier in RDS [51,52]. All these above spotlighted the contribution of asymmetric configuration induced by Co/Ru dual sites on thermodynamics and kinetics for urea electrosynthesis.

4. Conclusion

In this work, dual single-atom Ru and Co are stabilized on carbon nitride substrate through facile pyrolysis and established the asymmetric adsorption with CN intermediates via their selectivity differences towards C/N groups. The as-prepared $CoRuN_6$ electrocatalyst reveals outstanding activity with high urea yield rate of 8.98 mmol $h^{-1}g^{-1}$ and FE of 25.31% at − 0.6 V versus RHE. The in-situ spectroscopy dynamically discloses the double C-N coupling and multistage protonation process. Both the control experiment and theoretical calculations accentuate the prominent role of asymmetric configuration induced by dual sites on inhibiting side reactions (NO_3^-RR, CO_2RR), decreasing coupling barrier, and accelerating reaction kinetics. This research provides novel insights into utilizing spatial regulation between products and dual sites for efficient electrocatalytic urea synthesis.

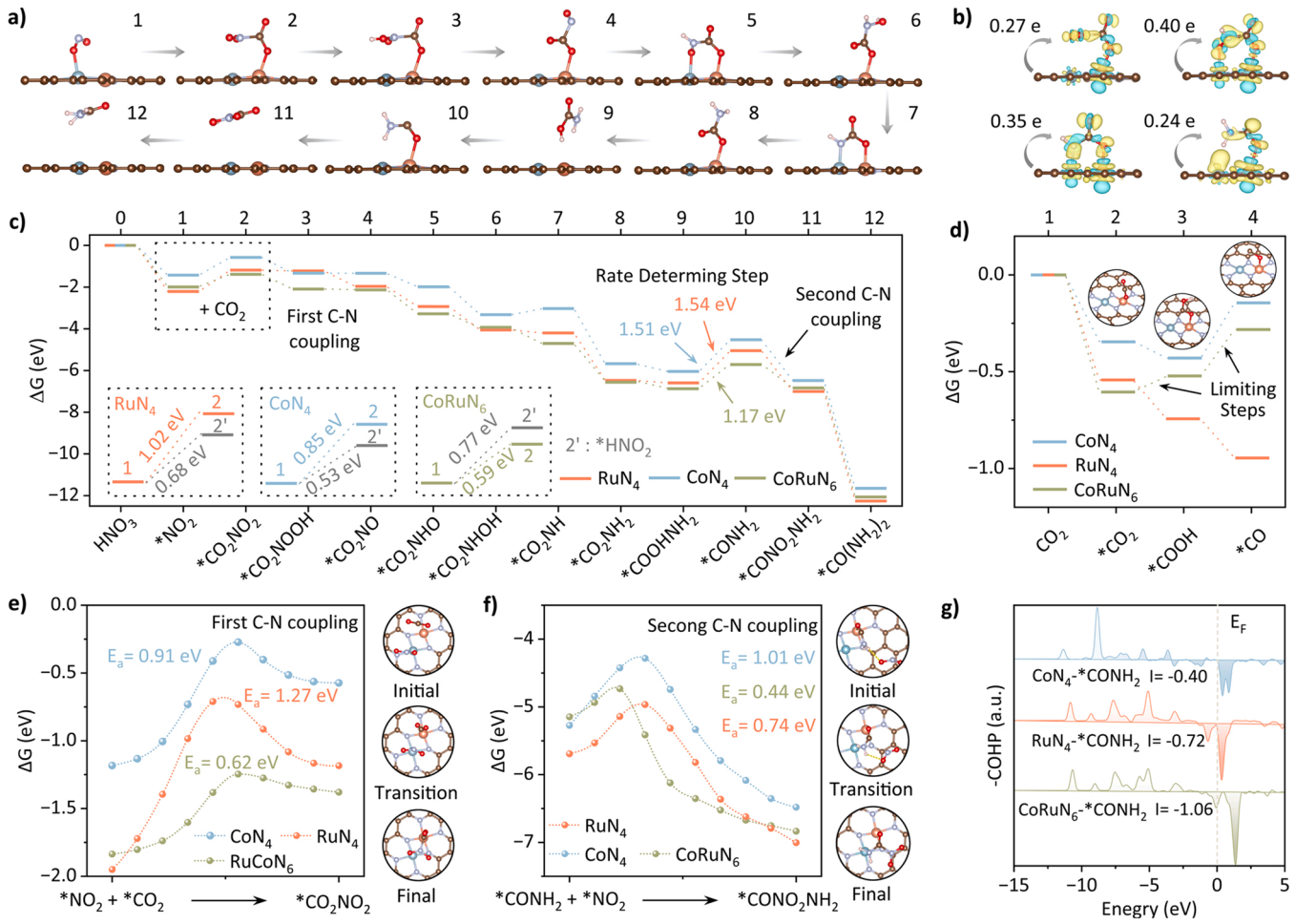

Fig. 5. (a) Optimized atomic configurations of each step for urea production using $CoRuN_6$. (b) Charge density difference of intermediates 2, 5, 7,10, (c) Free-energy diagram of different catalysts for urea production. (d) Free-energy diagram for CO_2 reduction, (e) The reaction pathway of first C-N coupling for $*CO_2NO_2$ formation and (f) second C-N coupling for $*CONO_2NH_2$ formation, accompanied by structures of the initial, transition and final states along reaction. (g) The crystal orbital Hamilton population (COHP) of $*CONH_2$ intermediate onto CoN_4, RuN_4 and $CoRuN_6$. (The orange, blue, red, silver, brown, and white balls represent Ru, Co, O, N, C, and H atoms, respectively).

CRediT authorship contribution statement

Chongchong Liu: Conceptualization, Methodology, Software, Investigation, Writing-original draft, Visualization. **Haili Tong:** Investigation, Writing - review & editing. **Peifang Wang:** Writing - review & editing. **Rong Huang:** Software, Investigation. **Peilin Huang:** Software, Visualization. **Gang Zhou:** Investigation, Supervision, review & editing. **Lizhe Liu:** Software, Visualization.

Declaration of Competing Interest

The authors declare that they have no known competing financial interests or personal relationships that could have appeared to influence the work reported in this paper.

Data Availability

No data was used for the research described in the article.

Acknowledgments

This work was supported by National Natural Science Foundation of China (92047201, 92047303, 52102237, 12174183), National Science Funds for Creative Research Groups of China (51421006). This work was supported by Natural Science Foundation of Jiangsu Province (BK20200516 and BK20220006), Postdoctoral Science Foundations of China and Jiangsu Province (2021M690861, 2022T150183, 2021K065A). This work was also supported by Fundamental Research Funds for the Central Universities (B220202062).

Appendix A. Supporting information

Supplementary data associated with this article can be found in the online version at doi:10.1016/j.apcatb.2023.122917.

References

[1] M. Aresta, A. Dibenedetto, A. Angelini, Catalysis for the valorization of exhaust carbon: from CO_2 to chemicals, materials, and fuels. technological use of CO_2, Chem. Rev. 114 (2014) 1709–1742, https://doi.org/10.1021/cr4002758.
[2] M. Yuan, J. Chen, Y. Xu, R. Liu, T. Zhao, J. Zhang, Z. Ren, Z. Liu, C. Streb, H. He, C. Yang, S. Zhang, G. Zhang, Highly selective electroreduction of N_2 and CO_2 to urea over artificial frustrated Lewis pairs, Energy Environ. Sci. 14 (2021) 6605–6615, https://doi.org/10.1039/D1EE02485J.
[3] D.B. Kayan, F. Köleli, Simultaneous electrocatalytic reduction of dinitrogen and carbon dioxide on conducting polymer electrodes, Appl. Catal. B Environ. 181 (2016) 88–93, https://doi.org/10.1016/j.apcatb.2015.07.045.
[4] M. Jiang, M. Zhu, M. Wang, Y. He, X. Luo, C. Wu, L. Zhang, Z. Jin, Review on electrocatalytic coreduction of carbon Dioxide and nitrogenous species for urea synthesis, ACS Nano (2023), https://doi.org/10.1021/acsnano.2c11046.
[5] M. Xia, C. Mao, A. Gu, A.A. Tountas, C. Qiu, T.E. Wood, Y.F. Li, U. Ulmer, Y. Xu, C. J. Viasus, J. Ye, C. Qian, G. Ozin, Solar urea: towards a sustainable fertilizer industry, Angew. Chem. 134 (2022), e202110158, https://doi.org/10.1002/ange.202110158.

[6] J. Fu, Y. Yang, J. Hu, Dual-sites tandem catalysts for C-N bond formation via electrocatalytic coupling of CO_2 and nitrogenous small molecules, ACS Mater. Lett. 3 (2021) 1468–1476, https://doi.org/10.1021/acsmaterialslett.1c00375.

[7] M. Jiang, Q. Zhu, X. Song, Y. Gu, P. Zhang, C. Li, J. Cui, J. Ma, Z. Tie, Z. Jin, Batch-scale synthesis of nanoparticle-agminated three-dimensional porous Cu@Cu_2O microspheres for highly selective electrocatalysis of nitrate to ammonia, Environ. Sci. Technol. 56 (2022) 10299–10307, https://doi.org/10.1021/acs.est.2c01057.

[8] C. Lv, L. Zhong, H. Liu, Z. Fang, C. Yan, M. Chen, Y. Kong, C. Lee, D. Liu, S. Li, J. Liu, L. Song, G. Chen, Q. Yan, G. Yu, Selective electrocatalytic synthesis of urea with nitrate and carbon dioxide, Nat. Sustain 4 (2021) 868–876, https://doi.org/10.1038/s41893-021-00741-3.

[9] M. Jiang, J. Su, X. Song, P. Zhang, M. Zhu, L. Qin, Z. Tie, J. Zou, Z. Jin, Interfacial reduction nucleation of noble metal nanodots on redox-active metal-organic frameworks for high-efficiency electrocatalytic conversion of nitrate to ammonia, Nano Lett. 22 (2022) 2529–2537, https://doi.org/10.1021/acs.nanolett.2c00446.

[10] X. Wei, X. Wen, Y. Liu, C. Chen, C. Xie, D. Wang, M. Qiu, N. He, P. Zhou, W. Chen, J. Cheng, H. Lin, J. Jia, X.-Z. Fu, S. Wang, Oxygen vacancy-mediated selective C-N coupling toward electrocatalytic urea synthesis, J. Am. Chem. Soc. 144 (2022) 11530–11535, https://doi.org/10.1021/jacs.2c03452.

[11] J. Geng, S. Ji, M. Jin, C. Zhang, M. Xu, G. Wang, C. Liang, H. Zhang, Ambient electrosynthesis of urea with nitrate and carbon dioxide over iron-based dual-sites, Angew. Chem. Int. Ed. 62 (2023), e202210958, https://doi.org/10.1002/anie.202210958.

[12] C. Chen, N. He, S. Wang, Electrocatalytic C-N coupling for urea synthesis, Small Sci. 1 (2021) 2100070, https://doi.org/10.1002/smsc.202100070.

[13] J. Leverett, T. Tran-Phu, J.A. Yuwono, P. Kumar, C. Kim, Q. Zhai, C. Han, J. Qu, J. Cairney, A.N. Simonov, R.K. Hocking, L. Dai, R. Daiyan, R. Amal, Tuning the coordination structure of Cu□N□C single atom catalysts for simultaneous electrochemical reduction of CO_2 and NO_3^- to Urea, Adv. Energy Mater. 12 (2022) 2201500, https://doi.org/10.1002/aenm.202201500.

[14] C. Lv, C. Lee, L. Zhong, H. Liu, J. Liu, L. Yang, C. Yan, W. Yu, H.H. Hng, Z. Qi, L. Song, S. Li, K.P. Loh, Q. Yan, G. Yu, A Defect engineered electrocatalyst that promotes high-efficiency urea synthesis under ambient conditions, ACS Nano 16 (2022) 8213–8222, https://doi.org/10.1021/acsnano.2c01956.

[15] X. Wei, Y. Liu, X. Zhu, S. Bo, L. Xiao, C. Chen, T.T.T. Nga, Y. He, M. Qiu, C. Xie, D. Wang, Q. Liu, F. Dong, C. Dong, X. Fu, S. Wang, Dynamic reconstitution between copper single atoms and clusters for electrocatalytic urea synthesis, Adv. Mater. (2023) 2300020, https://doi.org/10.1002/adma.202300020.

[16] X. Liu, P.V. Kumar, Q. Chen, L. Zhao, F. Ye, X. Ma, D. Liu, X. Chen, L. Dai, C. Hu, Carbon nanotubes with fluorine-rich surface as metal-free electrocatalyst for effective synthesis of urea from nitrate and CO_2, Appl. Catal. B Environ. 316 (2022), 121618, https://doi.org/10.1016/j.apcatb.2022.121618.

[17] D. Zhao, K. Yu, P. Song, W. Feng, B. Hu, W.-C. (Max) Cheong, Z. Zhuang, S. Liu, K. Sun, J. Zhang, C. Chen, Atomic-level engineering $Fe_1N_2O_2$ interfacial structure derived from oxygen-abundant metal–organic frameworks to promote electrochemical CO_2 reduction, Energy Environ. Sci. 15 (2022) 3795–3804, https://doi.org/10.1039/D2EE00878E.

[18] Z. Niu, S. Fan, X. Li, J. Duan, A. Chen, Interfacial engineering of CoMn2O4/NC induced electronic delocalization boosts electrocatalytic nitrogen oxyanions reduction to ammonia, Appl. Catal. B Environ. 322 (2023), 122090, https://doi.org/10.1016/j.apcatb.2022.122090.

[19] X. Cheng, J. He, H. Ji, H. Zhang, Q. Cao, W. Sun, C. Yan, J. Lu, Coordination symmetry breaking of single-atom catalysts for robust and efficient nitrate electroreduction to ammonia, Adv. Mater. 34 (2022) 2205767, https://doi.org/10.1002/adma.202205767.

[20] Z. Zhang, C. Liu, C. Feng, P. Gao, Y. Liu, F. Ren, Y. Zhu, C. Cao, W. Yan, R. Si, S. Zhou, J. Zeng, Breaking the local symmetry of $LiCoO_2$ via atomic doping for efficient oxygen evolution, Nano Lett. 19 (2019) 8774–8779, https://doi.org/10.1021/acs.nanolett.9b03523.

[21] J. Fu, J. Dong, R. Si, K. Sun, J. Zhang, M. Li, N. Yu, B. Zhang, M.G. Humphrey, Q. Fu, J. Huang, Synergistic effects for enhanced catalysis in a dual single-atom catalyst, ACS Catal. 11 (2021) 1952–1961, https://doi.org/10.1021/acscatal.0c05599.

[22] M. Li, H. Zhu, Q. Yuan, T. Li, M. Wang, P. Zhang, Y. Zhao, D. Qin, W. Guo, B. Liu, X. Yang, Y. Liu, Y. Pan, Proximity electronic effect of Ni/Co diatomic sites for synergistic promotion of electrocatalytic oxygen reduction and hydrogen evolution, Adv. Funct. Mater. 33 (2023) 2210867, https://doi.org/10.1002/adfm.202210867.

[23] T. Cui, Y. Wang, T. Ye, J. Wu, Z. Chen, J. Li, Y. Lei, D. Wang, Y. Li, Engineering dual single-atom sites on 2D ultrathin N-doped carbon nanosheets attaining ultra-low-temperature zinc-air battery, Angew. Chem. Int. Ed. 61 (2022), e202115219, https://doi.org/10.1002/anie.202115219.

[24] Y.-T. Xu, Y. Han, D.K. Sam, Y. Cao, The selective electrocatalytic reduction of nitrate to ammonia using Co(II)-decorated TiO_2 nanosheets, J. Mater. Chem. A. 10 (2022) 22390–22398, https://doi.org/10.1039/D2TA04707A.

[25] Y. Liu, T. Zhang, C. Deng, S. Cao, X. Dai, S. Guo, Y. Chen, Q. Tan, H. Zhu, S. Zhang, Y. Liu, Ordered mesoporous carbon spheres assisted Ru nanoclusters/RuO2 with redistribution of charge density for efficient CO_2 methanation in a novel H_2/CO_2 fuel cell, J. Energy Chem. 72 (2022) 116–124, https://doi.org/10.1016/j.jechem.2022.04.051.

[26] J. Hafner, Ab-initio simulations of materials using VASP: Density-functional theory and beyond, J. Comput. Chem. 29 (2008) 2044–2078, https://doi.org/10.1002/jcc.21057.

[27] V. Wang, N. Xu, J.C. Liu, G. Tang, W.T. Geng, VASPKIT: A user-friendly interface facilitating high-throughput computing and analysis using VASP code, Comput. Phys. Commun. 267 (2021), 108033, https://doi.org/10.1016/j.cpc.2021.108033.

[28] G. Henkelman, B.P. Uberuaga, H. Jónsson, A climbing image nudged elastic band method for finding saddle points and minimum energy paths, J. Chem. Phys. 113 (2000) 9901–9904, https://doi.org/10.1063/1.1329672.

[29] S. Maintz, V.L. Deringer, A.L. Tchougréeff, R. Dronskowski, LOBSTER: A tool to extract chemical bonding from plane-wave based DFT, J. Comput. Chem. 37 (2016) 1030–1035, https://doi.org/10.1002/jcc.24300.

[30] J. Liu, Z. Wei, Z. Gong, M. Yan, Y. Hu, S. Zhao, G. Ye, H. Fei, Single-atom CoN4 sites with elongated bonding induced by phosphorus doping for efficient H2O2 electrosynthesis, Appl. Catal. B Environ. 324 (2023), 122267, https://doi.org/10.1016/j.apcatb.2022.122267.

[31] J. Yi, X. Gao, H. Zhou, W. Chen, Y. Wu, Design of Co-Cu diatomic site catalysts for high-efficiency synergistic CO_2 electroreduction at industrial-level current density, Angew. Chem. Int. Ed. (2022), https://doi.org/10.1002/anie.202212329.

[32] G. Yang, J. Zhu, P. Yuan, Y. Hu, G. Qu, B.A. Lu, X. Xue, H. Yin, W. Cheng, J. Cheng, W. Xu, J. Li, J. Hu, S. Mu, J.-N. Zhang, Regulating Fe-spin state by atomically dispersed Mn-N in Fe-N-C catalysts with high oxygen reduction activity, Nat. Commun. 12 (2021) 1734, https://doi.org/10.1038/s41467-021-21919-5.

[33] H. Cheng, X. Wu, M. Feng, X. Li, G. Lei, Z. Fan, D. Pan, F. Cui, G. He, Atomically dispersed Ni/Cu dual sites for boosting the CO_2 reduction reaction, ACS Catal. 11 (2021) 12673–12681, https://doi.org/10.1021/acscatal.1c02319.

[34] Z. Pei, X.F. Lu, H. Zhang, Y. Li, D. Luan, X.W. (David) Lou, Highly efficient electrocatalytic oxygen evolution over atomically dispersed synergistic Ni/Co dual sites, Angew. Chem. 134 (2022), e202207537, https://doi.org/10.1002/ange.202207537.

[35] Y. Wang, K. Liu, J. Li, X. Yang, J. Hu, T.-S. Chan, X. Qiu, W. Li, M. Liu, CoN4 active sites in locally distorted carbon structure for efficient oxygen reduction reaction via regulating coordination environment, Chem. Eng. J. 429 (2022), 132119, https://doi.org/10.1016/j.cej.2021.132119.

[36] Z. Luo, X. Li, T. Zhou, Y. Guan, J. Luo, L. Zhang, X. Sun, C. He, Q. Zhang, Y. Li, X. Ren, Engineering energy level of FeN4 sites via dual-atom site construction toward efficient oxygen reduction, Small 19 (2023) 2205283, https://doi.org/10.1002/smll.202205283.

[37] Z. Wang, Z. Lin, J. Deng, S. Shen, F. Meng, J. Zhang, Q. Zhang, W. Zhong, L. Gu, Elevating the d-band center of six-coordinated octahedrons in Co9S8 through Fe-Incorporated topochemical deintercalation, Adv. Energy Mater. 11 (2021) 2003023, https://doi.org/10.1002/aenm.202003023.

[38] D. Deng, J. Qian, X. Liu, H. Li, D. Su, H. Li, H. Li, L. Xu, Non-covalent interaction of atomically dispersed Cu and Zn pair sites for efficient oxygen reduction reaction, Adv. Funct. Mater. 32 (2022) 2203471, https://doi.org/10.1002/adfm.202203471.

[39] M. Yuan, J. Chen, Y. Bai, Z. Liu, J. Zhang, T. Zhao, Q. Wang, S. Li, H. He, G. Zhang, Unveiling electrochemical urea synthesis by Co-activation of CO_2 and N_2 with Mott-Schottky heterostructure catalysts, Angew. Chem. Int. Ed. 60 (2021) 10910–10918, https://doi.org/10.1002/anie.202101275.

[40] Z. Yang, C. Zhao, Y. Qu, H. Zhou, F. Zhou, J. Wang, Y. Wu, Y. Li, Trifunctional self-supporting cobalt-embedded carbon nanotube films for ORR, OER, and HER triggered by solid diffusion from bulk metal, Adv. Mater. 31 (2019) 1808043, https://doi.org/10.1002/adma.201808043.

[41] M. Jiang, A. Tao, Y. Hu, L. Wang, K. Zhang, X. Song, W. Yan, Z. Tie, Z. Jin, Crystalline modulation engineering of Ru nanoclusters for boosting ammonia electrosynthesis from dinitrogen or nitrate, ACS Appl. Mater. Interfaces 14 (2022) 17470–17478, https://doi.org/10.1021/acsami.2c02048.

[42] L. Liu, H. Huang, Z. Chen, H. Yu, K. Wang, J. Huang, H. Yu, Y. Zhang, Synergistic polarization engineering on bulk and surface for boosting CO2 photoreduction, Angew. Chem. Int 60 (2021) 18303–18308, https://doi.org/10.1002/anie.202106310.

[43] R. Keuleers, H.O. Desseyn, B. Rousseau, C. Van Alsenoy, Vibrational analysis of urea, J. Phys. Chem. A 103 (1999) 4621–4630, https://doi.org/10.1021/jp984180z.

[44] M. Manivannan, S. Rajendran, Investigation of inhibitive action of Urea-Zn^{2+} system in the corrosion control of carbon steel in sea water, Int. J. Eng. Sci. Technol. 3 (2011) 8048–8060.

[45] J.A. Harvey, C.T. Johnston, L.J. Criscenti, J.A. Greathouse, Distinguishing between bulk and edge hydroxyl vibrational properties of 2: 1 phyllosilicates via deuteration, Chem. Commun. 55 (2019) 3453–3456, https://doi.org/10.1039/C9CC00164F.

[46] D. Yue, Y. Jia, Y. Yao, J. Sun, Y. Jing, Structure and electrochemical behavior of ionic liquid analogue based on choline chloride and urea, Electrochim. Acta 65 (2012) 30–36, https://doi.org/10.1016/j.electacta.2012.01.003.

[47] M. Jonusas, K. Leroux, L. Krim, N + H surface reaction under interstellar conditions: Does the $NH/NH_2/NH_3$ distribution depend on N/H ratio? J. Mol. Struct. 1220 (2020), 128736 https://doi.org/10.1016/j.molstruc.2020.128736.

[48] P. Zhu, X. Xiong, X. Wang, C. Ye, J. Li, W. Sun, X. Sun, J. Jiang, Z. Zhuang, D. Wang, Y. Li, Regulating the FeN4 moiety by constructing Fe–Mo dual-metal atom sites for efficient electrochemical oxygen reduction, Nano Lett. 22 (2022) 9507–9515, https://doi.org/10.1021/acs.nanolett.2c03623.

[49] C. Zhu, M. Wang, C. Wen, M. Zhang, Y. Geng, G. Zhu, Z. Su, Establishing the principal descriptor for electrochemical urea production via the dispersed dual-metals anchored on the N-decorated graphene, Adv. Sci. 9 (2022) 2105697, https://doi.org/10.1002/advs.202105697.

[50] L. Cheng, X. Yue, L. Wang, D. Zhang, P. Zhang, J. Fan, Q. Xiang, Dual-single-atom tailoring with bifunctional integration for high-performance CO_2 photoreduction, Adv. Mater. 33 (2021) 2105135, https://doi.org/10.1002/adma.202105135.
[51] Y. Gu, B. Xi, W. Tian, H. Zhang, Q. Fu, S. Xiong, Boosting selective nitrogen reduction via geometric coordination engineering on single-tungsten-atom catalysts, Adv. Mater. 33 (2021) 2100429, https://doi.org/10.1002/adma.202100429.
[52] W. Fu, Y. Du, J. Jing, C. Fu, M. Zhou, Highly selective nitrate reduction to ammonia on CoO/Cu foam via constructing interfacial electric field to tune adsorption of reactants, Appl. Catal. B Environ. 324 (2023), 122201, https://doi.org/10.1016/j.apcatb.2022.122201.